

**Beyond Darcy's law: The role of phase topology and ganglion dynamics for two-fluid flow**

Ryan T. Armstrong\*

*School of Petroleum Engineering, University of New South Wales, Sydney 2033, Australia*

James E. McClure

*Advanced Research Computing, Virginia Tech, Blacksburg, Virginia 24061, USA*

Mark A. Berrill

*Oak Ridge National Laboratory, Tennessee, Oak Ridge 37831, USA*

Maja Rücker

*Imperial College, London SW7 2AZ, United Kingdom*

Steffen Schlüter

*Helmholtz-Centre for Environmental Research - UFZ, Theodor-Lieser-Str. 4, 06120 Halle (Saale), Germany*

Steffen Berg

*Shell Global Solutions International B.V., Rijswijk, Kesslerpark 1, 2288 GS Rijswijk (Zh), The Netherlands*

(Received 23 June 2016; published 27 October 2016)

In multiphase flow in porous media the consistent pore to Darcy scale description of two-fluid flow processes has been a long-standing challenge. Immiscible displacement processes occur at the scale of individual pores. However, the larger scale behavior is described by phenomenological relationships such as relative permeability, which typically uses only fluid saturation as a state variable. As a consequence pore scale properties such as contact angle cannot be directly related to Darcy scale flow parameters. Advanced imaging and computational technologies are closing the gap between the pore and Darcy scale, supporting the development of new theory. We utilize fast x-ray microtomography to observe pore-scale two-fluid configurations during immiscible flow and initialize lattice Boltzmann simulations that demonstrate that the mobilization of disconnected nonwetting phase clusters can account for a significant fraction of the total flux. We show that fluid topology can undergo substantial changes during flow at constant saturation, which is one of the underlying causes of hysteretic behavior. Traditional assumptions about fluid configurations are therefore an oversimplification. Our results suggest that the role of fluid connectivity cannot be ignored for multiphase flow. On the Darcy scale, fluid topology and phase connectivity are accounted for by interfacial area and Euler characteristic as parameters that are missing from our current models.

DOI: [10.1103/PhysRevE.94.043113](https://doi.org/10.1103/PhysRevE.94.043113)**I. INTRODUCTION**

Many engineering applications depend fundamentally on multiphase flow through porous media. Hydrocarbon recovery, carbon sequestration, environmental contaminant transport, and fuel cell design are prominent examples. Understanding the multiscale relationships that determine the behavior of these systems is critical for many technologies. In geologic systems, transport processes often take place hundreds to thousands of meters below the Earth's surface, with fluids migrating similar distances [1]. Macroscale models are used to predict transport at these length scales, also known as the Darcy scale. At the Darcy scale, flow processes are described by averaged parameters, and microscopic details of the flow are neglected. These details include the configuration of fluid and solid phases at microscopic length scales where fluids are distributed in typically micrometer-sized pores in rock or other porous geologic material [2,3]. The configuration of the pore space and the fluids in it are complex, and topology can

vary widely from one material to another and for different flow regimes [4–6]. These properties can have a profound impact on transport at larger scales. In Fig. 1, we observe from our lattice Boltzmann simulations (as explained in Sec. II), that the movement of the disconnected nonwetting phase (NWP) occurs through a series of coalescence and snap-off events [7]. Videos of pore coalescence, snap-off, and ganglion dynamics are available in the Supplemental Material [8]. These pore-scale events have direct ramifications at the Darcy scale, since they can lead to entrapment and/or remobilization of the trapped NWP, as identified by researchers in the mid-1990s [9–11]. The influence of ganglion dynamics have been extensively studied in two-dimensional (2D) micromodels and using gradient percolation theory [12]; however, the identification of ganglion dynamics in 3D porous media has yet to be visualized and/or quantified other than a recent article that displays the influence that capillary number has on steady state relative permeabilities [13].

The fluid rearrangements shown in Fig. 1 occur during flow at fixed saturation, bringing into question the assumptions used to formulate our current macroscale flow equations that are entirely phenomenological. From a physics perspective,

\*ryan.armstrong@unsw.edu; <http://www.mutris.unsw.edu.au>

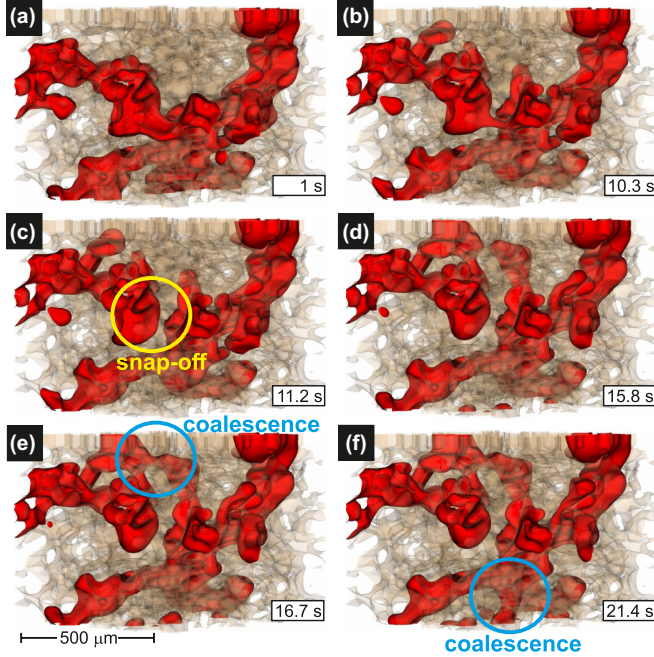


FIG. 1. Ganglion dynamics: snap-off and coalescence events result in continuously changing phase connectivity even at fixed saturation. The NWP is opaque whereas all other phases are transparent.

the big unresolved question is the consistent upscaling of multiphase flow in porous media from pore to continuum (Darcy) scale.

A two-phase extension of Darcy's law [14,15] is often used to model flow in geologic systems at the scale of several centimeters and above (Darcy scale). For an isotropic porous media, the formulation is

$$\phi \vec{v}_i = \frac{K k_i^r}{\mu_i} (\nabla p_i - \rho_i \vec{g}), \quad (1)$$

where the index  $i = w, n$  denotes the wetting ( $w$ ) and nonwetting ( $n$ ) phases,  $\vec{v}_i$  are the associated phase velocities,  $p_i$  are the fluid pressures,  $\rho_i$  are the phase densities,  $\mu_i$  are the phase viscosities, and  $\vec{g}$  is gravity. The effect of the solid geometry is accounted for by the porosity  $\phi$  and intrinsic permeability  $K$ , which quantifies the resistance to flow when only a single fluid is present. The relative permeabilities  $k_i^r$  account for all sub-Darcy scale physics, i.e., fluid-specific effects due to the arrangement of the two fluids in the system. The relative permeability for phase  $i$  is often written as

$$k_i^r = K_i / K, \quad (2)$$

where  $K_i$  is the effective permeability of phase  $i$ . The effective permeability predicts the ability of the porous material to conduct a particular phase when more than one phase is present, which should depend on the phase topology in the pore space. However, the relative permeability is often assumed to be a unique function of the wetting phase saturation  $S_w$ , supposing that each saturation is associated with a unique fluid configuration. Since the two-phase extension of Darcy's law is phenomenological, the precise dependencies for key parameters, e.g.,  $k_i^r(S_w)$ , are not clear. A recognized problem

with Eq. (1) is that the coefficients  $k_i^r$  are not unique functions of  $S_w$  [3,16]. For the same pair of fluids and porous media, different  $k_i^r(S_w)$  curves can be obtained depending on system history and flow rate [12,13,17]. The latter is sometimes parametrized via the dimensionless capillary number  $Ca$  [3], which is the ratio of viscous forces to capillary forces, defined as

$$Ca = \mu_w v_w / \gamma_{wn} \quad (3)$$

where  $\gamma_{wn}$  is the interfacial tension for the interface between the two fluids. As  $Ca$  increases the resulting relative permeabilities can change significantly.

A key goal of this work is to consider how fluid topology behaves at the microscale for a range of  $Ca$ , and to understand how these effects can be parametrized in a Darcy scale picture such as in Eq. (1). The results of integral geometry provide guidance in how to accomplish this objective. Three-dimensional structures can be characterized by four morphological descriptors denoted as Minkowski functionals ( $M_{0,1,2,3}$ ) that measure volume ( $M_0$ ), surface area ( $M_1$ ), integral mean curvature ( $M_2$ ), and integral Gaussian curvature ( $M_3$ ), which is equivalent to the Euler characteristic [4]. Traditional Darcy scale state variables include  $M_{0,1,2}$ , which relate to phase saturation ( $S_w$ ), specific interfacial area ( $A_{wn}$ ), and capillary pressure ( $P_c$ ), respectively [3,18,19]. However, when using the two-phase Darcy formulation [Eq. (1)] only phase saturation is considered; any effects due to changes in the remaining Minkowski functionals  $M_{1,2,3}$  are neglected. The implicit assumption is that phases flow through connected pathways and that interfaces between phases behave as rigid partitions [3], i.e.,  $M_{1,2,3}$  are constant at fixed saturation. However, observations of ganglion dynamics in experiments [20–22] and numerical simulation as displayed in Fig. 1 puts this view to question even for low capillary number flows [20].

Fast x-ray microcomputed tomography ( $\mu$ CT) experiments have made it possible to observe pore scale fluid configurations under dynamic flow conditions. This allows us to assess the assumption of connected pathway flow only, and to quantify the impact of pore scale displacements during flow on Darcy-scale flow parameters [23,24]. Recent computational advances make it now possible to couple experimentally observed geometries to pore-scale simulations. With this approach measurements and simulations can be carried out during fractional flow of oil and water at fixed saturation. During these flow processes the NWP and/or wetting phase (WP) can become disconnected. The disconnected phase may remain static or propagate through the pore space as individual ganglia [10,20,21]. Ganglion motion clearly is inconsistent with the view that interfaces behave as rigid partitions, which is an implicit assumption associated with the two-phase extension of Darcy's law. We observe that under specific flow conditions, disconnected NWPs move as a series of snap-off and coalescence events, which we characterize as ganglion dynamics (Fig. 1). Similar behavior has been identified in glass-etched pore networks [11]. Using simulation results, we measure the overall contribution of ganglion dynamics during fractional flow, and show that topological changes exert a significant influence on flow processes at fixed saturation and thus have a direct influence on the macroscopic system behavior.

TABLE I. TOMCAT beamline settings.

Option	Setting
FE filter	50%
OP-filter 1	100 $\mu\text{m}$ Al
Op-filter 2	40 $\mu\text{m}$ Cu
Op-filter 3	10 $\mu\text{m}$ Fe
Angular step	0.12
Lens magnification	3.08x
Camera	PCO.EDGE
Scintillator	100 $\mu\text{m}$ cerium-doped lutetium aluminum garnet

## II. MATERIALS AND METHODS

### A. Flow experiments

The sample was a water-wet, sintered glass sample called Robuglas with a porosity of 0.33, permeability of 22 Darcy, 4 mm diameter, and 20 mm length. The Robuglas sample has surface wetting characteristics, pore size distribution and wetting phase connectivity for corner flow similar to outcrop sandstone [25]. Dynamic high-resolution 3D images of fractional flow were collected at the TOMCAT beamline at the Swiss Light Source, Paul Scherrer Institut, Villigen, Switzerland. The images were collected at 36 KeV at a resolution of 4.22  $\mu\text{m}$ . Cesium chloride was used as the contrast agent and was added to the WP as a 1:6 weight ratio. A total of 1500 radiographs with 40-ms exposure times were collected for a single 3D image. Further details of the beam line settings are provided in Table I. The measured interfacial tension between decane and brine was 30 dyn/cm and the glass surface was assumed to be water wet after washing the sample with 3 pore volumes of toluene, ethanol, DI water, and last the CsCl brine solution.

Fractional flow is defined as

$$F_w = Q_w / Q_T, \quad (4)$$

where  $Q_w$  is the WP volumetric flow rate and  $Q_T$  is the total volumetric flow rate of WP and NWP. Water and decane were co-injected into the sample over a range of different fractional flows ( $F_w = 0.2, 0.5, \text{ and } 0.8$ ), i.e., similar to a steady state relative permeability measurement. Dynamic images were collected at each  $F_w$  during steady state flow, as indicated by pressure transducer readings. For a given  $F_w$ , once steady state was reached,  $Q_T$  was increased while maintaining constant  $F_w$ . We imaged fluid distributions at  $Q_T = 3, 30, \text{ and } 300 \mu\text{l}/\text{min}$  for each  $F_w$  tested to evaluate a range of different capillary numbers ( $\text{Ca} = 10^{-6}, 10^{-5}, \text{ and } 10^{-4}$ ). The pore-scale distributions of water and oil phases were obtained by segmenting the  $\mu\text{CT}$  images using gradient-based segmentation methods [26].

### B. Connected phase flow simulations

To assess the differences between connected pathway flow and ganglion dynamics, for the connected phase flow simulations only connected phases are considered and the phases are assumed to be separated by a rigid partition, i.e., all interfaces remain static (and also do not undergo

topological changes). We extract the phase arrangements for the connected WP and NWP experimental images and then simulate single phase flow using the lattice Boltzmann method (LBM) and thus the simulation and experimental data are at the same spatial resolution. We use a three-dimensional lattice with 19 possible momenta components (D3Q19) and the Bhatnager-Gross-Krook model; the same model has been used for the estimation of permeability in complex rock types [27]. For a given phase permeability, we set the phase-solid and phase-phase boundaries with a solid surface bounce back rule [28]. The resulting phase permeability (often referred to as effective permeability) is then normalized by the absolute permeability of the rock to obtain relative permeability. The absolute permeability is determined by running a single phase LBM simulation on the total pore space of the image. The same approach has been used elsewhere [29]. Therefore, the phase-phase boundaries are held constant, i.e., considered to act as rigid partitions with no topological changes, and the phase effective permeabilities of the connected phases are determined from the pore-scale experimental images.

### C. Two-fluid flow simulations

Segmented images were used to provide initial conditions for the phase geometry to perform steady-state simulations of fractional flow at fixed saturation. Two-fluid flow simulations were performed using a graphics processing unit-based implementation of the lattice Boltzmann method. The details of the implementation are provided by McClure *et al.* [30]. Additional details for the boundary condition used to set the contact angle are also available in the literature, demonstrating that the correct scaling is obtained for the dynamic behavior of the contact angle [31]. For the methods used, the thickness of the interface is approximately three voxel lengths. The image resolution (4.22  $\mu\text{m}$ ) was therefore sufficient to resolve essential aspects of the flow since the average pore diameter for the Robuglas sample is around 50  $\mu\text{m}$  [25]. We provide further credence to this statement by plotting the capillary pressure versus saturation curve obtained by LBM simulation in comparison to mercury intrusion porosimetry obtained from a sister plug of Robuglas (Fig. 2). The experimental and simulation results compare well for low capillary number flows and provide us confidence in our LBM results. The validation results also demonstrate a well established trend where capillary pressure increases with increasing capillary number [32]. This even further validates that the numerical methods provide results expected for dynamic conditions. We do not go into discussion of the results presented in Fig. 2, rather we present it as a validation step before presenting the main results and discussion.

An external force was used to drive the flow with full periodic boundary conditions. To avoid boundary effects, a periodic system was generated by reflecting the experimentally imaged geometry in the direction of flow. Simulations were performed under water-wet conditions. Various capillary numbers were simulated by varying the interfacial tension, the viscosity, and the magnitude of the force. The implementation is instrumented with *in situ* analysis capabilities to perform upscaling based on the microscale simulation state. The averaging framework was used to determine a variety of averages

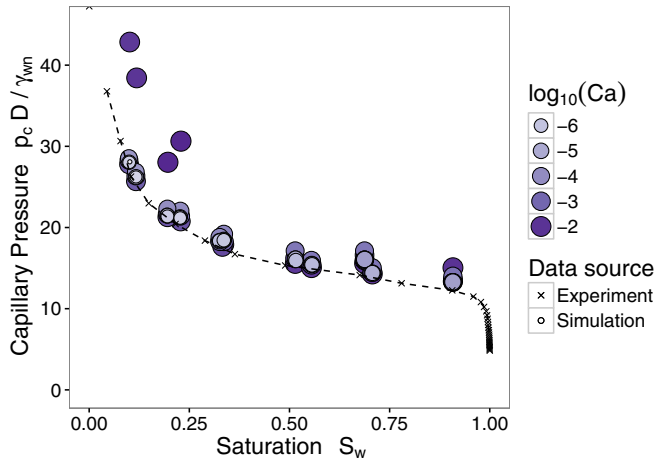


FIG. 2. Simulation and mercury intrusion porosimetry data for Robuglas compare well for low capillary number flows demonstrating that the image resolution was sufficient for LBM simulations.

over the phases, interfaces, and the common curve. Within this framework, macroscopic flow velocities were determined for each phase by computing the total momentum and dividing by the total mass. Additional quantities were also computed, including average phase pressures, average velocities for the interface and common curve, average mean curvature of the interface between fluids, and other measures defined from multiscale averaging theory [33]. A 4D connected components algorithm was used to identify and track each ganglion within the simulation. The coupling of experimentally obtained data with simulation provides access to parameters that cannot currently be directly measured during the experiment, i.e., nongeometric information, such as the phase pressure field, flow velocity field, flux associated with connected phase regions, and flux due to ganglion transport. The simulation approach is validated against experimental data by means of the Euler characteristic as a topological measure (details will be discussed in Sec. III C).

### III. RESULTS AND DISCUSSION

#### A. Relative permeability rate dependencies

Steady-state fractional flow experiments were conducted with a custom-built flow cell designed to collect 3D images at different fractional flow and Ca using state-of-the-art synchrotron-based fast  $\mu$ CT [23,24]. This allowed us to observe pore-scale fluid configurations during immiscible displacement. While the time resolution to collect a three-dimensional image is limited to many seconds, many fluid-fluid displacement mechanisms are known to occur at the ms time scale [34,35]. One such example is for Haines jumps where the NWP pressure increases enough for the NWP phase to pass through a pore throat and spontaneously fill the adjacent pore region [35]. Therefore lattice Boltzmann (LBM) simulations were used to complement the experiments to access these faster dynamics, and to infer the behavior of the fluid pressure and velocity field [30,33]. Observations of these dynamics can be seen in our LBM simulation, as provided in

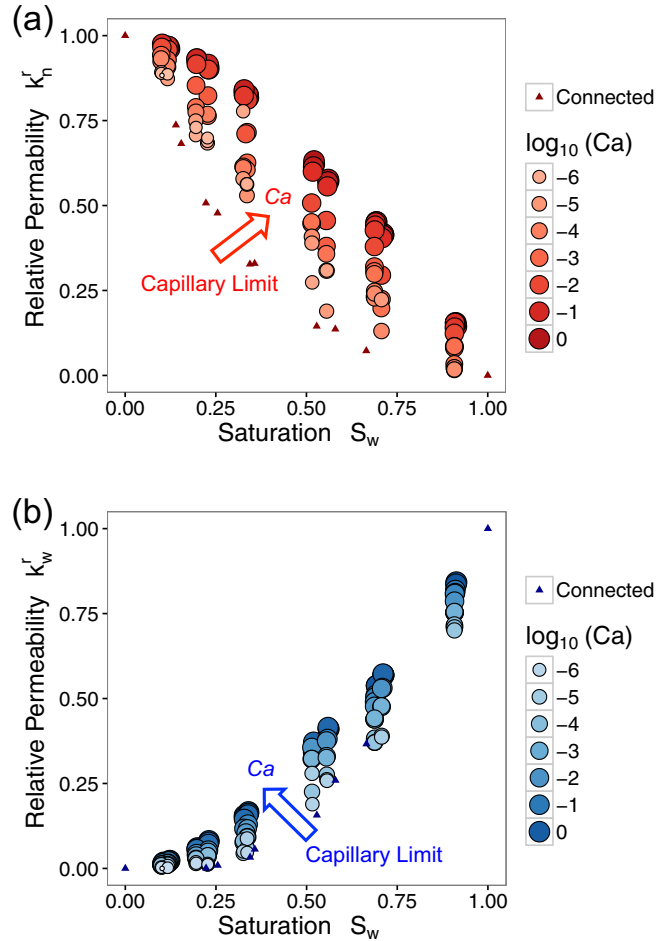


FIG. 3. Relative permeability values were determined for a wide range of Ca by initializing simulations from observed fluid configurations. Relative permeability values are higher than what is predicted from flow through rigid connected pathways. The implication is that dynamic changes to the phase topology leads to more efficient transport. NWP (a) and WP (b) relative permeabilities.

the Supplemental Materials S1 and S2 [8], where we observe a pore coalescence and snap-off event, respectively.

Initial conditions for the simulations were provided from 11 different fluid configurations observed during  $\mu$ CT fractional flow experiments in the same solid geometry. Each configuration corresponded to a different saturation value. First, the LBM was used to compute a steady-state solution to the Navier-Stokes equations under single-phase flow based on the solid geometry in order to determine the nondimensional intrinsic permeability,  $K/D^2 = 6.05 \times 10^4$ , with the Sauter mean diameter computed from the solid surface area and volume to be  $D = 317 \mu\text{m}$ . Second, single-phase simulations were performed in the connected portions of each fluid phase to predict the corresponding quasistatic relative permeabilities. These values correspond to the relative permeability obtained if the fluid interfaces behave as rigid partitions, and are plotted as triangles in Figs. 3(a) and 3(b) for the nonwetting and wetting fluids, respectively. Finally, two-phase flow simulations were initialized from the observed geometry to measure the relative permeability over a range of Ca. Periodic boundary

conditions were employed to ensure that relative permeabilities were measured at fixed saturation. Volume averaging was used to determine the macroscopic velocities for each phase, which were monitored to determine steady state. The simulated relative permeabilities are plotted as circles in Figs. 3(a) and 3(b), where we observe rate dependencies that are well aligned with the commonly accepted trends [3,12,13,17]. In particular, these relative permeability rate dependencies have been observed in micromodel experiments [11,13,17] and examined by numerical approaches [36,37]. We extend previous work by validating the behavior in a 3D porous system and our results demonstrate that the two-phase relative permeabilities under dynamic conditions exceed the values obtained in the quasistatic connected pathway limit for both fluids and all Ca. As seen in Supplemental Material S3, we observe ganglion dynamics from continuously changing phase connectivity during fractional flow at constant saturation [8]. Overall, These results indicate that dynamically changing pathways have a better transport efficiency than suggested by the traditional view of connected pathway flow.

**B. Preferred pathways for NWP ganglia**

Traditional approaches that assume relative permeability to be a function of only WP saturation cannot capture the observed relative permeability-rate dependencies. This should be expected given that phase saturation alone does not uniquely determine the wetting and NWP configurations during fractional flow. So, if phase saturation, i.e.,  $M_0$ , is held constant, how unique are the underlying phase configurations? We start to address this problem by looking at the population dynamics of NWP clusters as Ca is varied at constant saturation.

When a connected pathway exists, a clear separation in scales is evident when comparing the volumes of all connected components of the NWP. The NWP cluster size distribution is shown in Fig. 4 as a function of Ca for  $S_w = 0.51$ ,

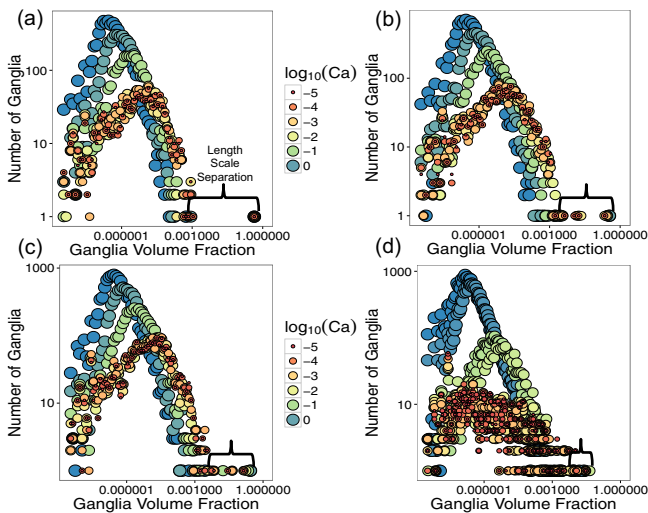


FIG. 4. The length scale separation between the largest cluster (connected pathway) and the larger population of smaller clusters decreases with increasing WP saturation. NWP ganglion size distributions for  $S_w = 0.51$  (a),  $S_w = 0.66$  (b),  $S_w = 0.71$  (c), and  $S_w = 0.91$  (d).

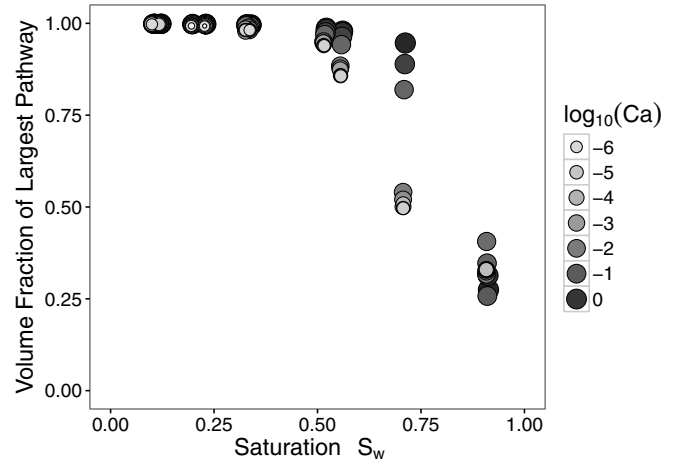


FIG. 5. The volume fraction of the largest pathway decreases with increasing WP saturation and increases with increasing capillary number except for the highest of WP saturation.

0.66, 0.71, and 0.91. Examining the distribution of volumes demonstrates that a single well-connected region of NWP is present, as are a large number of disconnected ganglia with much smaller volumes. Perhaps counterintuitively, while the size of individual ganglia decreases as Ca increases, the volume fraction associated with the connected pathway tends to increase, see Fig. 5, which shows the volume fraction of the largest connected pathway. This effect is due to the coalescence of ganglia with the much larger connected pathway. For many systems, trapped ganglia may not need to move very far before this occurs; a single Haines jump may be sufficient to reconnect a previously trapped ganglion with the main flow channel. As the flow rate increases, the frequency of Haines jumps also increases [34]. The effect is most prevalent for intermediate saturation values, where ganglion make up a significant fraction of the total NWP volume and a clear scale separation is observed between the ganglia and the connected pathway. Thus the existence of a preferred pathway for ganglia flow and increased rate of coalescence at high Ca allows for the development of cooperative transport of NWP through connected pathways, where the effective permeability of the NWP increases due to the evolution of its phase topology.

Our results suggest that higher Ca flows lead to topological changes that support more efficient flow processes at the Darcy scale. This occurs because fluid configurations that are inaccessible at low Ca are realized as the flow rate increases and capillary forces are less dominant. These effects are evident even when there is no connected pathway and all of the flux is due to ganglia flow. In this case, the disconnected ganglia become elongated as seen in Fig. 6. As the phase configuration changes, larger connected pathways may reconnect with previously immobile NWP ganglia. The changes observed at the pore scale point to the fundamental importance of phase connectivity in multiphase transport processes. To fully appreciate the consequence of these changes, we must incorporate relevant topological measures of connectivity at the macroscale.

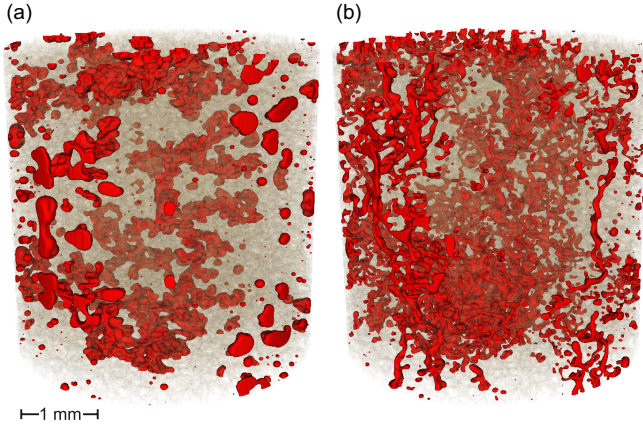


FIG. 6. Pore-scale images of NWP distribution (at  $S_w = 0.9$ ) for low (a)  $Ca = 3 \times 10^{-5}$ , and high (b)  $Ca = 3 \times 10^{-2}$ ,  $Ca$ . Oil ganglia coalesce and elongate in the direction of flow as the  $Ca$  increases, effects that lead to enhancement of the connected pathway. The NWP is opaque whereas all other phases are transparent.

### C. Relevance of fluid topology for phase permeability

Insights from the pore scale suggest that the causal connection between higher relative permeabilities and increased  $Ca$  are associated with topological changes in the NWP. With respect to topological measures, the effect of the volume is already included based on the dependence on  $S_w$ . Therefore, we focus attention on the interfacial area  $A_{wn}$  that has already been emphasized in [38] and the Euler characteristic  $\chi$ , which measures the phase connectivity. The Euler characteristic is a topological invariant defined as

$$\chi = \mathcal{N} - \mathcal{L} + \mathcal{O}, \quad (5)$$

where  $\chi$  is the Euler characteristic,  $\mathcal{N}$  is the number of objects,  $\mathcal{L}$  is the number of redundant connections or loops, and  $\mathcal{O}$  is the number of cavities. We focus on the Euler characteristic for the NWP, which is denoted by  $\chi_n$  and increases as the number of ganglia increases ( $\mathcal{N}$ ), and decreases as the NWP fills the pore space, i.e., leading to the formation of loops ( $\mathcal{L}$ ). In the context of percolation theory a Euler characteristic of 0 corresponds to a system near the percolation threshold; a negative Euler characteristic indicates a well-connected object, whereas a positive Euler characteristic indicates that an object is not well connected, such as when the NWP is fragmented [4]. Recent findings also indicate that different flow regimes exhibit characteristic differences in  $\chi_n$  due to very different fluid configurations even for the same  $S_w$  [4].

In Fig. 7, the Euler characteristic was determined from both simulated and experimental configurations, which is reported on a per-unit-volume basis to obtain an intensive quantity with units of  $\text{mm}^{-3}$ . For similar  $Ca$ , experimentally determined measurements show close agreement with simulation results and a very similar trend with saturation. This supports the conclusion that the geometries generated from simulation have phase connectivities that are similar to the experimentally observed systems. For  $S_w < 0.8$  the Euler characteristic decreases (becomes more negative) with increasing  $Ca$ , indicating an increase in NWP connectivity as new loops are formed in the pore space. For this saturation range

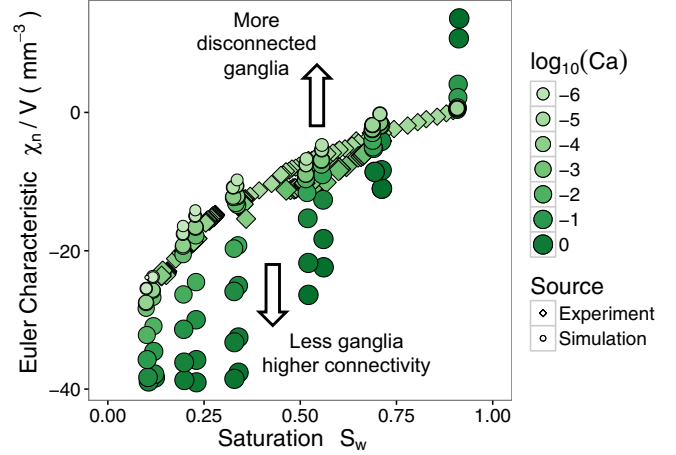


FIG. 7. The nondimensional Euler characteristic per unit volume measures changes in connectivity for the NWP. When a connected pathway is possible, experimental and simulated results show a trend toward enhanced connectivity (more negative Euler characteristic) as the  $Ca$  increases. When no connected pathway is possible, i.e.,  $S_w > 0.8$ , the Euler characteristic increases due to NWP fragmentation.

ganglion dynamics can enhance the connected pathways due to coalescence events. As a consequence, NWP becomes longer and larger as the  $Ca$  increases (see Fig. 6). The experimental data include  $Ca$  from approximately  $10^{-5}$  to  $10^{-3}$ , showing the same trend for enhanced connectivity at high  $Ca$ , and corroborating the simulation results. Interestingly at  $S_w > 0.8$  the trend is reversed and phase connectivity decreases with increasing  $Ca$ . For sufficiently high WP saturation there is no connected pathway present for ganglia to coalesce with and higher  $Ca$  leads to NWP fragmentation.

As a consequence of cooperative dynamics [34], ganglion flow can result in counterintuitive behavior. When the  $Ca$  is increased, the connectivity of NWP clusters also tends to increase. Intuitively, we might expect that as  $Ca$  increases NWP clusters would break apart and lead to higher Euler characteristic. However, this effect is only observed at the highest  $S_w$ , where a large number of NWP components are expected and no connected pathway is formed. For all other cases, we find that when  $Ca$  is increased (at constant  $S_w$ ) the NWP clusters become longer and larger, forming tubes that enhance connectivity. The fluid arrangements observed at high  $Ca$  would be impossible at lower flow rates, where capillary forces dominate and drive the NWP to larger pores where the surface energy is minimized, i.e., NWP becomes more spherical as presented in Fig. 6(a). This view challenges fundamental assumptions applied in up-scaling methods. First, the view that the saturation is sufficient to characterize microscale geometries is overtly insufficient. Second, approaches that assume disconnected NWP is trapped may not adequately describe flow processes at high wetting saturation, particularly when larger  $Ca$  are encountered. The coexistence of connected pathway flow and ganglion dynamics means that theories must account for the interdependence of these flow mechanisms; approaches that treat connected pathway flow and ganglion dynamics separately will be subject to inherent limitations. We find that for a wide range of saturation there exists a prevalent

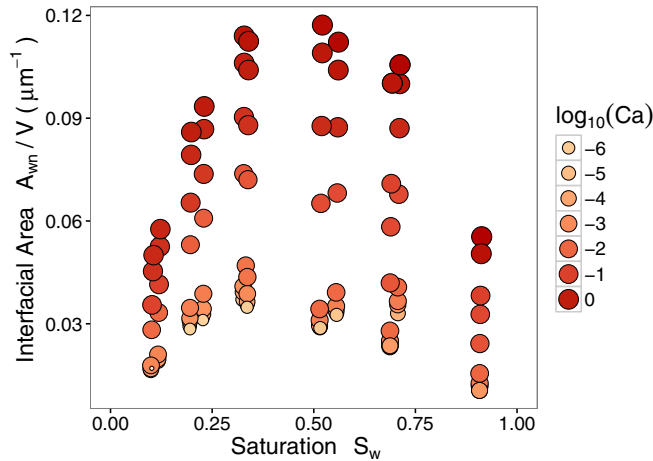


FIG. 8. Specific interfacial area increases as the NWP transitions to the elongated connected pathways that form with increasing capillary number.

rate dependence and that the underlying topology of phases are changing in significant ways.

The reason for topological changes as  $\text{Ca}$  is increased can be further understood by looking at the interfacial area between the wetting and NWP. The specific interfacial area is the surface area of the interface between wetting and NWP divided by system volume. This is reported in Fig. 8 for a range of  $\text{Ca}$  and saturation values. Since the interfacial energy increases with  $A_{wn}$ , increases in the interfacial area tend to occur once capillary forces are less dominant. The value of  $A_{wn}$  plotted in Fig. 8 corresponds to the specific Euler characteristic measured in Fig. 7 and relative permeabilities measured in Fig. 3. In contrast to  $\chi_n$ , increasing  $\text{Ca}$  results in an increase to  $A_{wn}$  for all saturation values. The interfacial area between phases increases as the NWP transitions to elongated “thin” connected pathways. A transition seems to take place around  $\text{Ca} = 10^{-3}$  where both  $\chi_n$  and  $A_{wn}$  change significantly. Presumably this would be the result once viscous (and possibly inertial) forces become stronger than capillary forces. The simulation accounts for the balance of forces at the pore scale. As evident from Figs. 7 and 8, fluid-fluid interfaces start to significantly rearrange around  $\text{Ca} = 10^{-3}$ , which would only occur if local forces are large enough to deform the interfaces and move them. The topology may then stabilize to some extent at higher  $\text{Ca}$  after this transition occurs. This possibility is supported by the fact that the relative permeability values seem to stabilize for  $\text{Ca} > 10^{-3}$ .

During ganglion dynamics, fluid configurations change continuously as individual ganglia move through the pore space. This requires that interfaces deform and move as the displacement occurs. Nevertheless, measurements of the relative permeability, interfacial area, and Euler characteristic suggest that these configurations lead to very similar average topological and flow properties, particularly if large systems with many ganglia are considered. This suggests that average topological properties may be sufficient to predict relative permeability, even for cases where fluid configurations are continuously changing at the microscale. This provides a path forward for theory that can be supported by existing

experimental and simulation methods, since topology is now an accessible parameter that influences macroscale transport.

**D. Flux contribution of ganglion dynamics**

The boundary between phases can no longer be considered as a rigid partition. This has been a widely debated concept that recent researchers have suggested to be correct [21], which we show conclusively. The connected phase pathways continuously evolve due to the prevailing physical forces and disconnected phases continuously merge and disconnect from the connected pathway. But to what extent does the disconnected NWP contribute to the overall NWP flux? Does bulk transport of NWP occur mostly through the connected pathway flow or through the movement of disconnected NWP? The answer to these questions is relevant to how we consistently move across scales from pore-scale displacement to Darcy-scale formulations. Considering that ganglion flux is a less efficient means of oil transportation, e.g., nearly 2/3 of the total work of drainage is considered dissipative due to interfacial jumps [23,39], it is critical to understand the percentage of phase flux that occurs through connected pathway flow versus ganglion dynamics.

A “phase diagram” summarizing the  $\text{Ca}-S_w$  space is presented in Fig. 9, which quantifies the relative flux contribution of ganglion dynamics in comparison to the total NWP flux. The black circles represent simulation results from which the figure is generated using a spline interpolation method. Also, the color of each circle is the true color that represents the measured ganglion flux. When a connected pathway exists, this part of the NWP will also tend to be the largest feature, by volume fraction. This is based on the scale separation observed in Fig. 4. We therefore define the ganglion flux as the portion of the flux not associated with the largest feature. Connected pathway flow and ganglion dynamics flow regimes coexist over

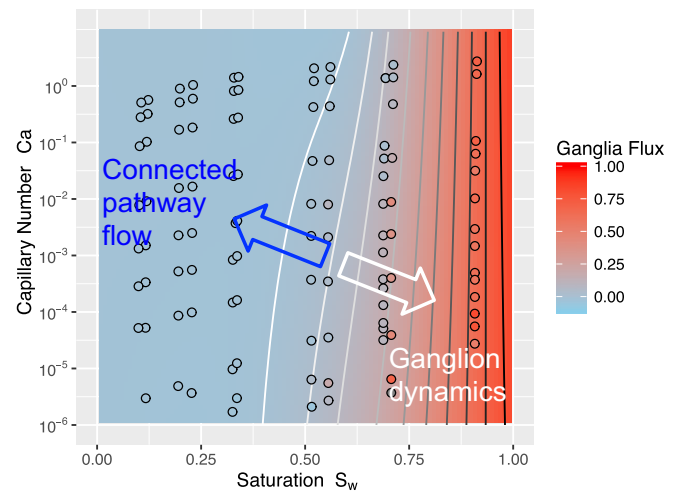


FIG. 9. Flux associated with ganglia disconnected from the largest feature (by vol.) increases as wetting phase saturation increases. At intermediate saturation values, ganglion flux decreases with increasing  $\text{Ca}$  due to NWP coalescence, re-establishing connected pathway flow. The circles are simulation results from which the figure is generated and the color is the true value from the measured ganglion flux.

a wide range of saturation and Ca without a sharp transition between regimes. We observe a gradual increase in ganglion flux as  $S_w$  increases for all Ca. This is expected, since the NWP is less well connected as  $S_w$  increases, which is clear from Fig. 7.

A less intuitive result is that the ganglion flux decreases as Ca increases for intermediate saturation values. This is a consequence of the fact that the size of the connected pathway grows due to coalescence as Ca increases. This enhanced connectivity is also clear from Fig. 7. For  $S_w < 0.5$  nearly all of the NWP flux is contained in the largest connected component of the phase, which is the connected pathway; see Fig. 5. For  $S_w > 0.5$ , a significant fraction of the NWP flux is contained in many smaller disconnected ganglia. As the fraction of NWP contained in the largest ganglion increases, so too does the contribution of the ganglia to the overall NWP flux. While ganglia exist for smaller  $S_w$ , the contribution of the movement of the disconnected phases is negligible compared to the flow that occurs in the largest cluster. By contrast at  $S_w = 0.71$ , approximately 10–25% of the total NWP flux is due to the movement of ganglia. The transition from connected to disconnected phase flow occurs gradually, evident from Fig. 9, and depends on the topology of the porous medium and the capillary number.

It may be possible to identify the flow regimes by examining the variation of relative permeability and Ca using core-scale experiments, as discussed in a recent publication [13]. In theory, this should be possible by adjusting Ca and measuring fluxes; however, obviously we cannot distinguish between connected and disconnected phase flux. Also, there are experimental artifacts that complicate this approach. In particular, the capillary-end effect, i.e., capillary pressure equal to zero at the end of the core, can lead to rate dependencies similar to ganglion dynamics; while researchers have developed experimental approaches to overcome these effects [40–43] this complication is not fully resolved. Local heterogeneity in rock samples can also result in similar rate dependencies, e.g., see [44]. These effects are significant when measuring experimental rate dependencies, which our simulations using a homogeneous material and cyclic boundary conditions are not influenced by. To better understand rate dependencies at the core scale, we first need to evaluate the effect using numerical simulations on various rock types, as provided herein. Last, we use fractional flow experiments and simulations since this is a common approach for steady state relative permeability measurements and it is easy to implement fractional flow cyclic boundary conditions with LBM. However, a significant contribution of ganglion flux due to snapoff, coalescence, and mobilization is also expected for directional flows and countercurrent flows.

### E. Implications for engineering applications

NWP trapping and mobilization mechanisms are of great interest to the oil and gas industry since these mechanisms impact oil recovery efficiency. Standard oil recovery technologies leave  $\geq 50\%$  of the original oil in place in the oil reservoir due to reservoir heterogeneity and pore-scale trapping [45]. Understanding the mobility of this trapped oil is critical for enhanced oil recovery (EOR) operations. These effects also

play a role for storage operations where supercritical  $\text{CO}_2$  is trapped in a reservoir. In the context of  $\text{CO}_2$  sequestration it is important to evaluate the fate of  $\text{CO}_2$  injected into a formation over geological time. Trapped  $\text{CO}_2$  will typically be disconnected, i.e.,  $S_w > 0.5$ , and ganglia mobilization is therefore important. As WP saturation increases the NWP becomes disconnected [7] and thus nonpercolating. In traditional trapping models, once the NWP is disconnected it is considered to be immobile [46]. We find that depending on the flow conditions and phase topology, disconnected NWP can still be mobile. For many geologic systems, a wide range of Ca can be encountered. Near a well, where flow rates are higher, high Ca effects may be important. Also, significant density differences can arise in brine- or oil- $\text{CO}_2$  systems which may lead to buoyancy forces that overcome capillary forces and result in mobilization of  $\text{CO}_2$  [47]. Relative permeability hysteresis has been shown to influence the long-term trapping of  $\text{CO}_2$  in geologic sequestration operations [48]. Our results suggest that models that do not account for the potential mobilization of “trapped”  $\text{CO}_2$  underestimate the relative permeability, particularly for WP saturation between 0.5 and 0.75 where both ganglion dynamics and connected pathway transport are likely to occur. Furthermore, widely used trapping models are parametrized in terms of the saturation only [46]. Our results show that at fixed saturation, disconnected portions of the NWP can reconnect with connected pathway as Ca increases. As a consequence, the trapped portions of NWP cannot be considered a unique function of fluid saturation. Furthermore, we show that the mobilization of disconnected NWP is a potentially important phenomenon over a fairly wide range of WP saturation. These findings suggest that macroscale models that assume disconnected phases are permanently trapped will tend to underpredict the mobility of  $\text{CO}_2$  in geologic sequestration applications. A more complete topological characterization of the phase configurations represents a promising alternative to existing theoretical approaches.

Overall the results suggest that saturation alone does not uniquely define fluid flow. Additional topological measurements, such as the Euler characteristic, are required. For extending Darcy’s law, we must recognize that this is the case. There is no theoretical basis for why relative permeability should depend on saturation only. It is essentially a first-order assumption that works relatively well and is easy to measure. However, for complex flow physics, i.e., high Ca flows, additional second-order terms such as Euler characteristic can be considered. From the standpoint of nondimensional analysis, relative permeability is a dimensionless quantity and may depend on other dimensionless quantities, e.g., saturation, Euler characteristic, or capillary number. Recent attempts are underway to explore the links between fluid connectivity, topology, and resulting flow behavior [4].

## IV. SUMMARY AND CONCLUSIONS

Insights obtained by combining fast  $\mu\text{CT}$  with advanced simulations will facilitate the development of new Darcy-scale theories for the flow of immiscible phases through porous media that are consistent with pore scale displacement physics. Understanding the role of topology will be at the forefront of multiphase flow research and reduce inconsistencies between



pore-scale and Darcy-scale formulations. We discovered that ganglion dynamics is an important transport mechanism that explains relative permeability rate dependencies. We quantified the flux of connected and disconnected NWP and demonstrate that connected pathway flow is a poor assumption even for relatively low Ca flows. Often, rate dependencies are attributed to experimental artifacts, rock heterogeneity when larger scale systems are considered, and/or the time derivative of WP saturation. However, we clearly demonstrate rate dependencies in uniform porous media at constant saturation. For relative permeability, we find phase topology to be the controlling parameter and it is dependent on saturation and Ca. Phase topology can evolve, at constant saturation, during fractional flow depending on the flow conditions and the resulting effect has macroscale implications. Our results demonstrate that (1) the traditional two-phase Darcy formulation has contributions originating from connected pathway flow and from dissipative pore-scale events; (2) these two flow regimes coexist during fractional flow; and (3) the Euler characteristic provides a way to characterize the connectivity of the flow regimes at the macroscale. For example in a recent statistical description of multiphase flow [49], the Euler characteristic is used to represent configurational entropy, which provides a way forward to incorporate the fluid topology into Darcy-scale thermodynamic models. Overall, these findings provide a way

to address fundamental limitations associated with traditional Darcy-scale multiphase flow formulations, which impacts a wide range of engineering applications.

#### ACKNOWLEDGMENTS

X-ray microcomputed tomography was performed on the TOMCAT beamline at the Swiss Light Source, Paul Scherrer Institute, Villigen, Switzerland. An award of computer time was provided by the Innovative and Novel Computational Impact on Theory and Experiment (INCITE) program. This research also used resources of the Oak Ridge Leadership Computing Facility, which is a DOE Office of Science User Facility supported under Contract No. DE-AC05-00OR22725.

This manuscript has been supported by UT-Battelle, LLC under Contract No. DE-AC05-00OR22725 with the U.S. Department of Energy (DOE). The publisher, by accepting the article for publication, acknowledges that the United States Government retains a nonexclusive, paid-up, irrevocable, world-wide license to publish or reproduce the published form of this manuscript, or allow others to do so, for U.S. Government purposes. The DOE will provide public access to these results of federally sponsored research in accordance with the DOE Public Access Plan.

- 
- [1] F. M. Orr, *Science* **325**, 1656 (2009).
- [2] S. Iglauer, A. Paluszny, C. H. Pentland, and M. J. Blunt, *Geophys. Res. Lett.* **38**, L21403 (2011).
- [3] F. A. L. Dullien, *Porous Media Fluid Transport and Pore Structure* (Academic Press Limited, New York, 1991).
- [4] S. Schlüter, S. Berg, M. Rücker, R. Armstrong, H.-J. Vogel, R. Hilfer, and D. Wildenschild, *Water Resour. Res.* **52**, 2194 (2016).
- [5] A. L. Herring, L. Andersson, S. Schlüter, A. Sheppard, and D. Wildenschild, *Adv. Water Resour.* **79**, 91 (2015).
- [6] A. L. Herring, E. J. Harper, L. Andersson, A. Sheppard, B. K. Bay, and D. Wildenschild, *Adv. Water Resour.* **62**, 47 (2013).
- [7] J. Roof, *SPE J.* **10**, 85 (1970).
- [8] See Supplemental Material at <http://link.aps.org/supplemental/10.1103/PhysRevE.94.043113> for a video of a pore coalescence event, a video of a pore snap-off event, and a video of ganglion dynamics.
- [9] D. G. Avraam, G. B. Kolonis, T. C. Roumeliotis, G. N. Constantinides, and A. C. Payatakes, *Transp. Porous Media* **16**, 75 (1994).
- [10] D. G. Avraam and A. C. Payatakes, *Ind. Eng. Chem. Res.* **38**, 778 (1999).
- [11] D. G. Avraam and A. C. Payatakes, *Transp. Porous Media* **20**, 135 (1995).
- [12] C. D. Tsakiroglou, M. A. Theodoropoulou, and V. Karoutsos, *AIChE J.* **49**, 2472 (2003).
- [13] C. Tsakiroglou, C. Aggelopoulos, K. Terzi, D. Avraam, and M. Valavanides, *Int. J. Multiphase Flow* **73**, 34 (2015).
- [14] J. Bear and Y. Bachmat, *Introduction to Modeling of Transport Phenomena in Porous Media* (Springer Science and Business Media, 1991).
- [15] H. Darcy, *Les Fontaines Publiques de la Ville de Dijon* (Dalmont, Paris, 1856).
- [16] H. Li, C. Pan, and C. T. Miller, *Phys. Rev. E* **72**, 026705 (2005).
- [17] C. Tsakiroglou, D. Avraam, and A. Payatakes, *Adv. Water Resour.* **30**, 1981 (2007).
- [18] R. J. Held and M. A. Celia, *Adv. Water Resour.* **24**, 325 (2001).
- [19] M. L. Porter, D. Wildenschild, G. Grant, and J. I. Gerhard, *Water Resour. Res.* **46**, W08512 (2010).
- [20] M. Rücker, S. Berg, R. T. Armstrong, A. Georgiadis, H. Ott, A. Schwing, R. Neiteler, N. Brussee, A. Makurat, L. Leu, M. Wolf, F. Khan, F. Enzmann, and M. Kersten, *Geophys. Res. Lett.* **42**, 3888 (2015).
- [21] S. S. Datta, T. S. Ramakrishnan, and D. A. Weitz, *Phys. Fluids* **26**, 022002 (2014).
- [22] S. S. Datta, J.-B. Dupin, and D. A. Weitz, *Phys. Fluids* **26**, 062004 (2014).
- [23] S. Berg, H. Ott, S. A. Klapp, A. Schwing, R. Neiteler, N. Brussee, A. Makurat, L. Leu, F. Enzmann, J.-O. Schwarz, M. Kersten, S. Irvine, and M. Stampanoni, *Proc. Natl. Acad. Sci. U. S. A.* **110**, 3755 (2013).
- [24] R. T. Armstrong, H. Ott, A. Georgiadis, M. Rücker, A. Schwing, and S. Berg, *Water Resour. Res.* **50**, 9162 (2014).
- [25] S. Berg, R. Armstrong, H. Ott, A. Georgiadis, S. Klapp, A. Schwing, R. Neiteler, N. Brussee, A. Makurat, L. Leu *et al.*, *Petrophysics* **55**, 304 (2014).
- [26] S. Schlüter, A. Sheppard, K. Brown, and D. Wildenschild, *Water Resour. Res.* **50**, 3615 (2014).
- [27] C. H. Arns, F. Bauguet, A. Limaye, A. Sakellariou, T. J. Senden, A. P. Sheppard, R. M. Sok, W. V. Pinczewski, S. Bakke, L. I. Berge, P. E. Oeren, and M. A. Knackstedt, *SPE J.* **10**, 475 (2005).
- [28] N. S. Martys and H. Chen, *Phys. Rev. E* **53**, 743 (1996).

- [29] S. Berg, M. Rücker, H. Ott, A. Georgiadis, H. van der Linde, F. Enzmann, M. Kersten, R. Armstrong, S. de With, J. Becker *et al.*, *Adv. Water Resour.* **90**, 24 (2016).
- [30] J. McClure, J. Prins, and C. Miller, *Comput. Phys. Commun.* **185**, 1865 (2014).
- [31] J. McClure, M. Berrill, W. Gray, and C. Miller, *J. Fluid Mech.* **796**, 211 (2016).
- [32] S. M. Hassanizadeh, M. A. Celia, and H. K. Dahle, *Vadose Zone J.* **1**, 38 (2002).
- [33] J. E. McClure, H. Wang, J. F. Prins, C. T. Miller, and W. C. Feng, in *IEEE 28th International Symposium on Parallel and Distributed Processing* (IEEE, Piscataway, NJ, 2014), pp. 583–592.
- [34] R. T. Armstrong and S. Berg, *Phys. Rev. E* **88**, 043010 (2013).
- [35] W. B. Haines, *Studies in the Physical Properties of Soils* (Cambridge University Press, 1930).
- [36] M. Valavanides and A. Payatakes, *Adv. Water Resour.* **24**, 385 (2001).
- [37] G. N. Constantinides and A. C. Payatakes, *AIChE J.* **42**, 369 (1996).
- [38] S. Hassanizadeh and W. G. Gray, *Adv. Water Resour.* **13**, 169 (1990).
- [39] N. R. Morrow, *Ind. Eng. Chem. Res.* **62**, 32 (1970).
- [40] R. Gupta and D. Maloney, in *International Symposium of the Society of Core Analysts, Canada, 16–21 August, 2015*.
- [41] G. Hadley, L. Handy *et al.*, in *Fall Meeting of the Petroleum Branch of AIME* (Society of Petroleum Engineers, Los Angeles, California, 1956), pp. 14–17.
- [42] D. D. Huang and M. M. Honarpour, *J. Pet. Sci. Eng.* **19**, 103 (1998).
- [43] F. Hussain, Y. Cinar, and P. Bedrikovetsky, *Transp. Porous Media* **92**, 187 (2012).
- [44] C. Reynolds, M. Blunt, and S. Krevor, *Energy Procedia* **63**, 5577 (2014).
- [45] L. W. Lake, *Enhanced Oil Recovery* (Prentice Hall, 1989).
- [46] C. Land, *SPE J.* **8**, 149 (1968).
- [47] M. L. Szulczewski, C. W. MacMinn, H. J. Herzog, and R. Juanes, *Proc. Natl. Acad. Sci. U. S. A.* **109**, 5185 (2012).
- [48] R. Juanes, E. J. Spiteri, F. M. Orr, and M. J. Blunt, *Water Resour. Res.* **42**, W12418 (2006).
- [49] J. Xu and M. Y. Louge, *Phys. Rev. E* **92**, 062405 (2015).